

Multi-objective design optimization of 3D micro-architected implants

Garner, E.; Wu, J.; Zadpoor, A.A.

DOI

[10.1016/j.cma.2022.115102](https://doi.org/10.1016/j.cma.2022.115102)

Publication date

2022

Document Version

Final published version

Published in

Computer Methods in Applied Mechanics and Engineering

Citation (APA)

Garner, E., Wu, J., & Zadpoor, A. A. (2022). Multi-objective design optimization of 3D micro-architected implants. *Computer Methods in Applied Mechanics and Engineering*, 396. <https://doi.org/10.1016/j.cma.2022.115102>

Important note

To cite this publication, please use the final published version (if applicable). Please check the document version above.

Copyright

Other than for strictly personal use, it is not permitted to download, forward or distribute the text or part of it, without the consent of the author(s) and/or copyright holder(s), unless the work is under an open content license such as Creative Commons.

Takedown policy

Please contact us and provide details if you believe this document breaches copyrights. We will remove access to the work immediately and investigate your claim.



Multi-objective design optimization of 3D micro-architected implants

Eric Garner^a, Jun Wu^{b,*}, Amir A. Zadpoor^a

^a Department of Biomechanical Engineering, Delft University of Technology, Mekelweg 2, Delft, 2628 CD, The Netherlands

^b Department of Sustainable Design Engineering, Delft University of Technology, Landbergstraat 15, Delft, 2628 CE, The Netherlands

Received 16 February 2022; received in revised form 29 April 2022; accepted 30 April 2022

Available online 23 May 2022

Abstract

Recent advances in 3D printable micro-architected materials offer unprecedented possibilities for the development of highly tailored orthopaedic implants. These devices, which are typically made from fully solid materials, significantly alter load transmission to the surrounding bone tissue, potentially leading to interface instability and bone resorption. In this work, we present computational methods to synthesize three dimensional (3D), patient-specific, implants with heterogeneous micro-architecture. Our method simultaneously minimizes the risks of load-induced interface fracture and peri-prosthetic bone remodelling, while taking into account functional and manufacturing constraints.

We first develop a novel parametric micro-architecture with desirable functional attributes and a wide range of effective mechanical properties, including both positive and negative Poisson's ratios. We then present formulations which optimize the spatial configuration of micro-architecture parameters in order to simultaneously minimize the risk of load-induced interface fracture and post-operative bone remodelling. To that end, a novel bone remodelling objective is devised, taking into account both bone apposition and resorption, predicted via a model based on strain–energy density. The interface fracture objective is defined as the maximum value of the multi-axial Hoffman failure criterion along the interface.

The procedure is applied to the design of 3D titanium hip implants with prescribed conventional geometries and compared, *in silico*, to both a conventional solid implant and a homogeneous low-stiffness lattice design. The optimized implant results in a performance improvement of 64.0% in terms of bone remodelling, and 13.2% in terms of interface fracture risk, compared to a conventional solid implant design.

© 2022 The Author(s). Published by Elsevier B.V. This is an open access article under the CC BY license (<http://creativecommons.org/licenses/by/4.0/>).

Keywords: Topology optimization; Additive manufacturing; Bone remodelling; Stress shielding; Interface fracture; Heterogeneous lattice

1. Introduction

New developments in the fields of additive manufacturing and micro-architected materials offer an opportunity to produce mechanical components with unprecedented geometric complexity. This design freedom, in turn, enables engineers to design components which greatly outperform their conventionally engineered counterparts. However, the design of these new micro-architected components requires a thorough understanding of the use context, as well as the development of novel computational methods. In this work, we present multi-objective optimization methods for the design of orthopaedic hip implant stems in an effort to improve their longevity and avoid the

* Corresponding author.

E-mail addresses: e.garner@tudelft.nl (E. Garner), j.wu-1@tudelft.nl (J. Wu), A.A.Zadpoor@tudelft.nl (A.A. Zadpoor).

need for complicated revision surgeries. We demonstrate the superior performance of these optimized designs over conventional solid and uniform lattice designs *in silico*, via finite element analysis.

Orthopaedic implant stems used in total hip arthroplasty (THA) are typically fully solid and made from engineering materials, such as titanium alloys, stainless steel, chromium alloys, or tantalum. These materials have been selected for their high strength, relatively low density, corrosion resistance, and biocompatibility. Although considerable strides have been made towards improving long-term implant fixation and osseointegration, 15% of THA patients undergo revision surgery within 10 years, of which over half are required within the first 5 years [1,2]. Revisions are more complex due to degradation of the peri-prosthetic bone tissue and represent a four-fold increase in failure risk, compared to the original procedure [3]. Although patient-related medical factors play a role in bone resorption, mechanical, rather than medical factors are believed to be responsible for most bone-related implant failure [4]. From a mechanical perspective, two main factors contribute to peri-prosthetic bone degradation: *inadequate stress transmission to the bony tissue*, and *inappropriate stress conditions along the bone-implant interface*.

Orthopaedic implants are typically made from much stiffer materials (100–200 GPa) [5] than the relatively compliant bone tissue (14.8–20.7 GPa) [6]. As a result of this mismatch, much of the loads applied to the implant are not transmitted to the surrounding bone tissue. This phenomenon, known as stress shielding, triggers bone remodelling, which is an adaptive process through which bone is deposited or resorbed based on local stress conditions [7]. Over time, the reduced stress conditions result in significant bone resorption. This phenomenon, termed bone loss secondary to stress shielding, can lead to serious complications, such as aseptic loosening, chronic pain, and peri-prosthetic fracture.

In the last few decades, numerous strategies have been proposed to reduce stress shielding. A common approach has been to reduce the difference in stiffness between the implant and bone tissue. Means to achieving that end fall into two categories: modification of the implant geometry and the use of low-stiffness materials. Geometric modifications include alteration of the implant cross-section [8–10], stem length reduction [11–13], stem hollowing [14,15], and the addition of anchors, collars or grooves [8,10,16]. Material modifications include the use of polymeric composites or porous metals [17–19], metallic foams [20,21], and cellular structures [22]. However, the introduction of softer materials has the undesired effect of increasing the risk of interface failure by producing considerably higher tensile and shear stresses [19,23]. Fracture of the relatively weak interface leads to aseptic loosening, alters load transmission to the surrounding bone tissue and produces wear particles, which can lead to bone resorption and further aseptic loosening [24].

Kuiper and Huiskes were first to identify the conflict between stress shielding and interface instability. In their seminal work, they introduced the notion of an implant with spatially-varying mechanical properties and proposed a multi-objective optimization strategy which was successful in reducing both stress shielding and the risk of stress-related interface fracture. Their work, however, was limited to the optimization of a coarse 2D model and considered only the macro-scale problem [25,26]. Arabnejad and Pasini extended upon their idea by additionally considering the micro-scale detail, making use of genetic algorithms to improve the design of a 3D-printable implant with parametric micro-architecture [27]. Other contributions have mostly focused on the stress shielding aspect. Some authors have proposed metrics to quantify bone resorption or stress shielding, while others have used compliance as a surrogate [28–30]. These methods have proven successful in reducing stress shielding, but suffer from a number of shortcomings (e.g., regarding sensitivity to tuning parameters, which will be further discussed in the methodology section).

In industry, despite early concerns regarding fatigue failure [31], porous materials, such as metallic foams [20,21], porous tantalum [32] and open-cell porous coatings [22] are gaining traction. Their structure allows for increased bone ingrowth and interface strengthening. However, their success is strongly dependent on pore size, porosity and mechanical conditions — factors which can be difficult to control independently of one another [33–35]. Instead, recent advances in additive manufacturing technologies, such as selective laser sintering (SLS), selective laser melting (SLM), and electron-beam melting (EBM), have enabled the precise fabrication of functional components with ultra-fine detail using advanced engineering materials, such as titanium alloys and stainless steel [36]. These advances are expected to enable the fabrication of implants with custom micro-architecture, offering extremely precise control over the porosity, pore size, and mechanical properties [37–40].

To take full advantage of the newly expanded design space, however, efficient computational methods are critical. Until now, studies have been limited to a small number of design variables and relatively coarse finite

element discretization. These concessions were necessary due to the high computational costs associated with the proposed optimization strategies. On the other hand, in the field of topology optimization, gradient-based non-linear optimization strategies, such as the method of moving asymptotes (MMA) [41], as well as efficient finite element solvers, such as multi-grid preconditioned conjugate gradient [42,43] have been specifically designed to handle finite element analysis problems with thousands or millions of design variables, facilitating the timely solution of large 3D optimization problems on a standard PC. These methods can be applied to the design of multi-scale structures with both micro-scale and macro-scale considerations [44–48]. We refer to a recent review article for an overview of multi-scale topology optimization methods [49].

In this work, we propose a gradient-based numerical optimization methodology to automatically synthesize 3D micro-architected implants that simultaneously minimize the risk of interface fracture and implant-induced bone remodelling. The procedure decouples the micro-scale unit-cell geometry from the macro-scale design problem, allowing for the efficient inclusion of manufacturing and/or application-related constraints, while significantly reducing the computational costs compared to concurrent multi-scale strategies. In addition, we propose performance metrics which, we argue, more accurately represent the design objectives than in prior publications. We validate our method by comparing the optimized design, in its full micro-architectural detail, with a solid implant and one with uniform lattice.

The remainder of this paper is organized as follows. We first present an overview of the design methodology. Next, we describe the parametric micro-architecture. This is followed by an explanation of the optimization objectives and constraints. Finally, the optimization strategy is applied to the design of 3D hip implant stems under multiple loading conditions, the results of which are summarized and discussed in detail.

2. Methodology

The structure of our three-stage method is presented in Fig. 1. In stage 1, a parametric micro-architecture is defined and evaluated via numerical homogenization to extract its effective properties. In stage 2, the macro-scale implant design problem is formulated based on patient-specific bone data. In stage 3, the implant optimization problem is solved using the design space defined in stage 1. This section provides detail on each stage.

2.1. Parametric micro-architecture

The first stage of our implant design method involves the definition and characterization of a parametric micro-architecture for use in a decoupled multi-scale optimization formulation. In such a formulation, the micro-scale architecture design is decoupled from the macro-scale optimization. This approach reduces computation costs, but introduces the possibility of poor compatibility between adjacent unit cells with different micro-architecture. A number of strategies have been proposed to address these issues, though these methods tend to incur significant computation cost [48–53]. Instead, we introduce a parametric micro-architecture, such that adjacent cell compatibility and smoothly varying geometric properties can be ensured at a negligible computational cost.

To be suitable for use with our implant optimization formulation, the parametric micro-architecture must be able to produce a wide and smoothly varying range of mechanical properties. Moreover, it must possess adjacent cell connectivity and open-cell porosity, and must be suited to additive manufacturing. To these ends, we propose a generalization of the well-known cubic anti-chiral topology. It possesses the required attributes and can produce both positive and negative (auxetic) Poisson's ratios, a rare feature which has been recently utilized in the design of hip implant stems [54,55].

The generalized cubic anti-chiral topology, shown in Figs. 2 and 3, is characterized by a set of identical sinusoidal curves with amplitude a and diameter d , both defined as a fraction of the unit cell side-length. For small diameter values, negative values of a correspond to the familiar auxetic structure, while positive values of a correspond to a different structure resembling close-packed spheres, and results in positive Poisson's ratios ν , greater than that of the base material ν_0 . Note that the curves are at 45° from the principle planes to ensure that the mechanical properties are identical in the principle directions. Parameter a is, in fact, the amplitude projected onto the face of the cubic bounding box, as shown in Fig. 3. The diameter parameter, d , controls the effective elastic modulus. By tuning these two parameters within the design space, a wide range of mechanical properties can be achieved. The aforementioned design space is defined to ensure a non-overlapping geometry, which can be written as $4a - 2d \leq 1$. If additional geometric constraints are imposed, the design space is reduced accordingly. For each additional constraint, values

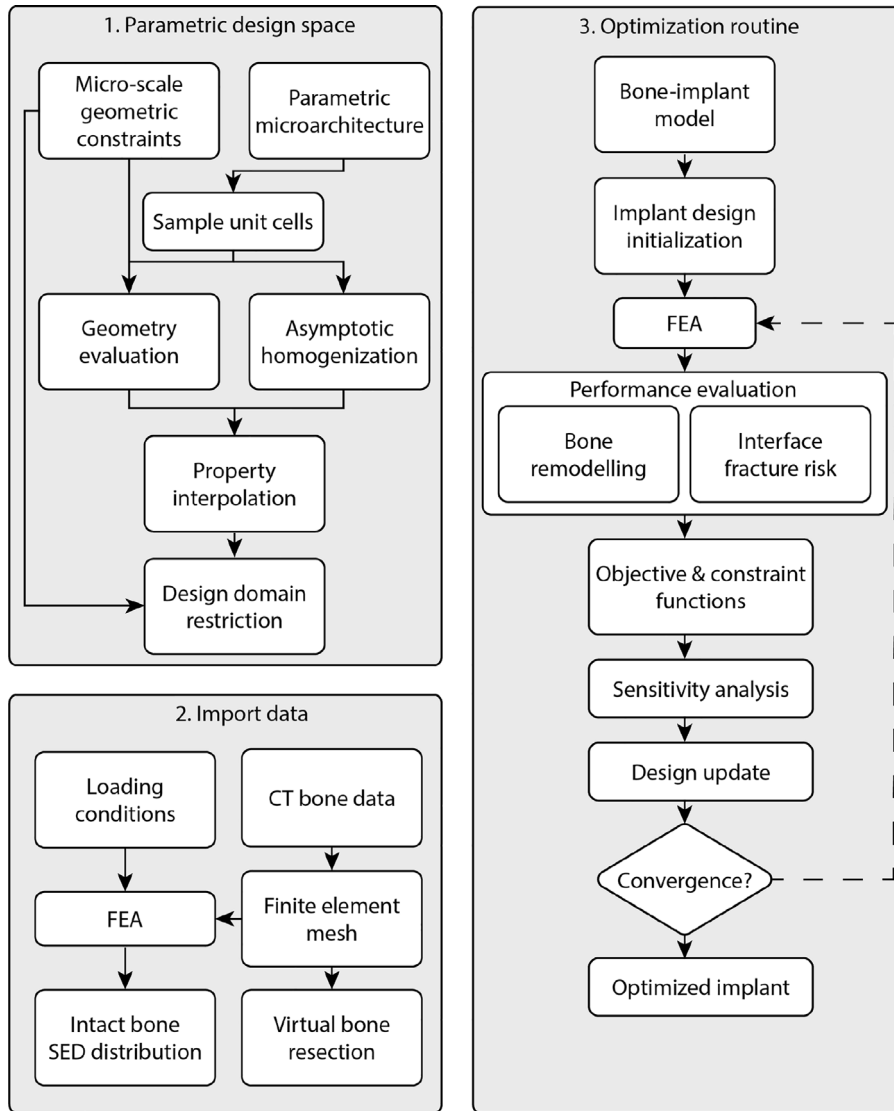


Fig. 1. Flow chart illustrating our approach for the design of micro-architected material (1), initialization (2) and optimization (3) procedures.

are computed for a set of sample micro-architecture. From there, a binary mask Φ_c is generated and applied to the original design space Φ :

$$\Phi_{constrained} = \Phi \cap \Phi_{c_1} \cap \dots \cap \Phi_{c_m} \tag{1}$$

where Φ_{c_i} is the binary mask associated with constraint i , and m is the number of added constraints. This method allows for the inclusion of any number of geometry-related constraints, without incurring additional computational cost. Fig. 4 shows the original and reduced design spaces when maximum effective density and minimum length scale are imposed.

In order to facilitate an efficient optimization procedure, we do not represent the implant in its full micro-architectural detail. Instead, we take advantage of the quasi-periodic nature of our structure and employ asymptotic homogenization (AH) to map from each geometric parameter combinations to a corresponding homogenized elasticity tensor.

In many cases, multi-scale approaches involve repeated AH of each micro-architecture, for every design iteration. This costly procedure is necessary when the micro-architecture topology is not prescribed. In this case, however,

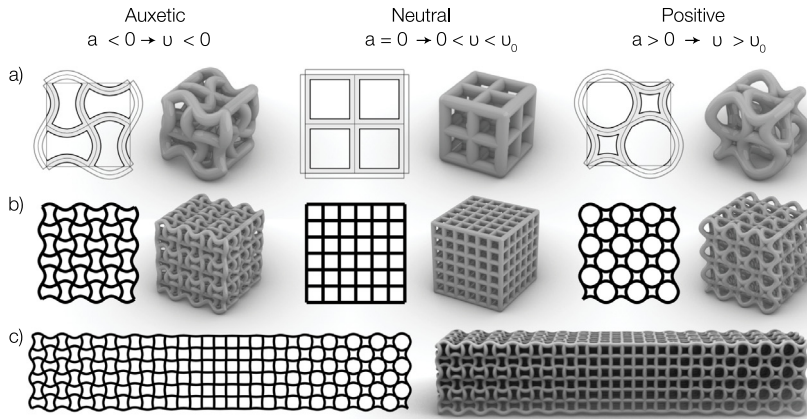


Fig. 2. Generalized parametric cubic anti-chiral micro-architecture: (a) Sample unit cells exhibiting negative, neutral, and positive Poisson's ratios; (b) Periodic arrays of unit cells (c) A functionally graded assembly of chiral micro-architectures exhibiting ideal interface connectivity. The left-hand side illustrations refer to the 2D version of the structure, while the right-hand side illustrations refer to the 3D version shown in Fig. 3, and used throughout this work.

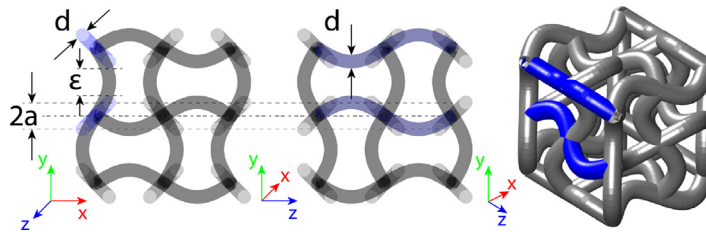


Fig. 3. An illustration of the 3D cubic anti-chiral micro-architecture, shown in the front, side, and isometric views, including the geometric design parameters a and d . ϵ represents the clearance between adjacent wave forms. The highlighted blue wave forms on the right correspond to the highlighted blue out-of-plane wave forms on the left. (For interpretation of the references to colour in this figure legend, the reader is referred to the web version of this article.)

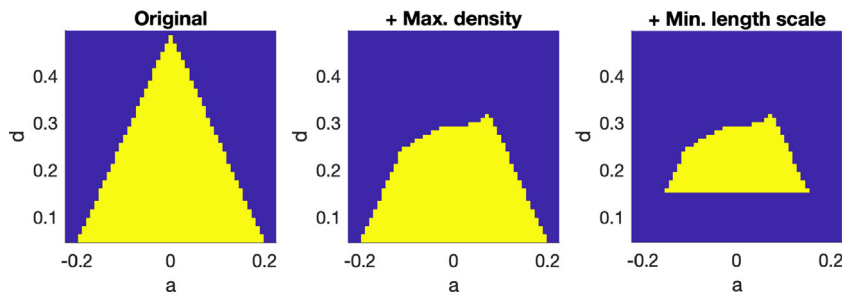


Fig. 4. Design space Φ without constraint (left), including maximum density constraint (middle), including maximum density and minimum length scale constraints (right).

re-evaluation via AH can be avoided by characterizing the entire space of possible geometric parameter combinations prior to optimization. To that end, we evaluate a set of 1600 representative volume elements (RVE) spanning the range of geometric properties. Samples were discretized using between $60 \times 60 \times 60$ and $100 \times 100 \times 100$ hexahedral finite elements and homogenized using the method described in [56]. The higher resolution was used for samples with small d values, in order to ensure mesh independence. This procedure was performed in ~ 100 hours on a standard PC with a 2.6 GHz 6-core Intel i7 CPU. From there, cubic interpolation is used to capture the relations between the geometric and mechanical properties. The effective properties for any feasible parameter combination

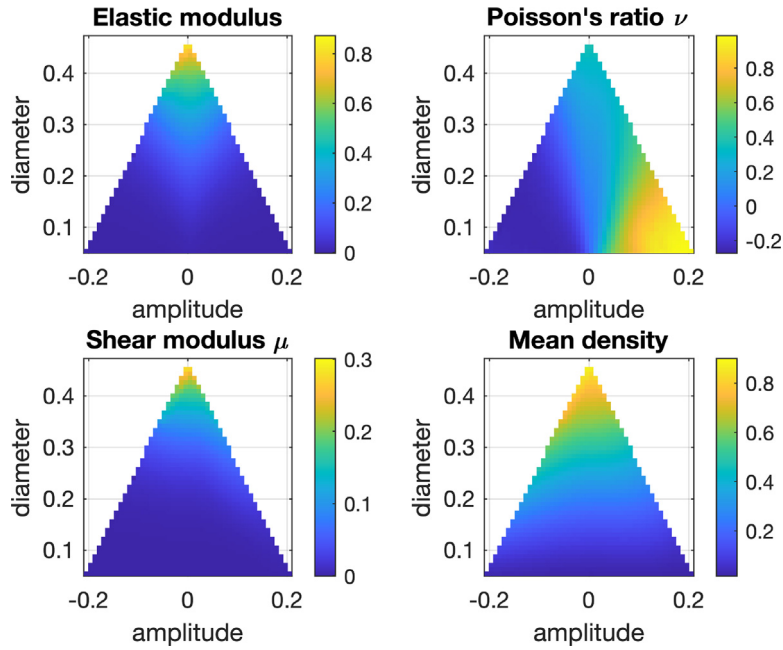


Fig. 5. Normalized mechanical properties obtained via asymptotic homogenization and fitted using cubic surface interpolation.

can be obtained by simple interpolation, rather than expensive AH. The fitted functions mapping the geometric parameter combinations to the effective elastic modulus, Poisson's ratio, and shear modulus are shown in Fig. 5, each normalized with respect to the elastic modulus of the bulk material.

2.2. Finite element model

The bone geometry and density information used in this work is that of a 28 year old healthy male patient, obtained via computational tomography (CT) and retrieved from the embodi3D database [57]. The CT data is projected onto the finite element mesh, along with the density information. The bone boundaries are then extracted using the marching cubes algorithm, and used to enrich the finite element model, according to the extended finite element method outlined below. The original and resected bone meshes are shown in Fig. 6, along with the density information. The loading conditions are based on the walking and stair climbing profiles described in [58], with slight modifications to fit the bone model (see Appendix for details). Note that in this work, the implant is not preloaded, as it would be when press-fitted into place. This simplification most likely causes an overestimation of the interface fracture risk and bone resorption. As a result, the optimized design's predicted performance will be somewhat conservative.

The bone-implant system is represented on a $158 \times 158 \times 210$ mm fixed grid with $2 \times 2 \times 2$ mm trilinear hexahedral elements using an extended finite element method (XFEM). The XFEM model captures discontinuities in the displacement field by enriching a set of nodes along the interface with additional degrees of freedom (DOF) and interpolating them with discontinuous shape functions. This allows for a more accurate representation of the physical geometry and captures discontinuities in the displacement, strain, and stress fields. Both features improve the accuracy of interface stress predictions over standard fixed grid methods, while maintaining low computational costs. For completeness, the XFEM procedure is briefly introduced here.

According to the XFEM strategy, elements which are cut by a material interface are enriched with additional degrees of freedom (see Fig. 7). Specifically, each DOF associated with a node belonging to a cut element is duplicated. The added DOF is associated with a discontinuous shape function, thus enabling discontinuities in the displacement field. The displacement $\mathbf{u}(\mathbf{x})$ at any point \mathbf{x} on either side of the interface is obtained from the standard

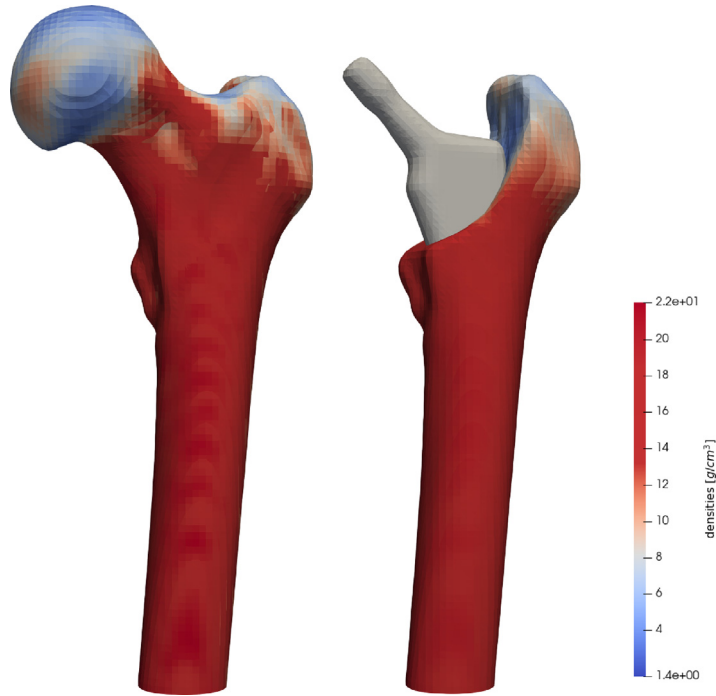


Fig. 6. Original (left) and resected (right) bone geometries, and density distributions, projected to the extended finite element mesh.

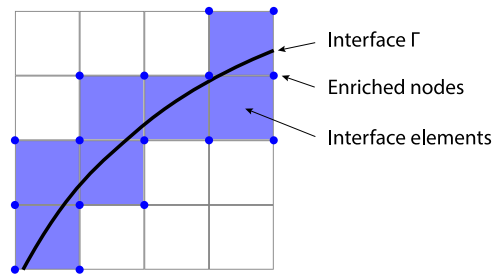


Fig. 7. XFEM enrichment along material interface.

and enriched element DOF solutions **a** and **b**:

$$\mathbf{u}_e(\mathbf{x}) = \sum_{i \in D} N_i(\mathbf{x})\mathbf{a}_i + \sum_{j \in \Gamma} \nu(\mathbf{x})N_j(\mathbf{x})\mathbf{b}_j \tag{2}$$

where N_i and N_j are the conventional shape functions. The enrichment function $\nu(\mathbf{x})$ is here defined as

$$\nu(\mathbf{x}) = H(\phi(\mathbf{x})) - H(\phi(\mathbf{x}_j)) \tag{3}$$

in which $\phi(\mathbf{x})$ is the level set function equal to zero along the interface Γ , \mathbf{x}_j is the coordinate of node j , and $H(\phi(\mathbf{x}))$ is the Heaviside function of the level set ϕ at coordinate \mathbf{x} . This second order discontinuous shape function captures the discontinuities of the strain field, assuming a perfectly bonded interface. A detailed description of the XFEM strategy can be found in [59].

2.3. Bone remodelling

To assess the performance of an implant design, we consider two main failure mechanisms: failure at the interface due to inappropriate stress conditions, and excessive bone resorption due to stress shielding. Bone loss can be most

accurately predicted via a bone remodelling simulation. However, these simulations involve computationally heavy iteration. Instead, a number of alternative formulations have sought to approximate bone loss by considering the stress conditions immediately before and after THA. Kuiper and Huiskes proposed to count up the amount of bone which is locally under-stressed [25]. Specifically,

$$m_r(\mathbf{b}) = \frac{1}{M} \int_V g(S(\mathbf{b})) \rho dV \quad (4)$$

where M and V are the original bone mass and volume, respectively, and $g(S(\mathbf{b}))$ is a resorptive function equal to unity if the local strain energy density S is below a certain threshold, defined in terms of the original strain energy density S_{ref} . This function, though commonly referenced and employed in the literature [27,60], suffers from a vulnerability. Since it does not differentiate between a slightly under-loaded and an extremely under-loaded local stress condition, the optimization routine cannot prioritize one over another. Moreover, this function is highly sensitive to the choice of threshold value and may incorrectly evaluate the quality of an implant under certain conditions. For instance, a design for which a slight under-loading exists throughout the bone would be considered poorer than a design for which extreme bone loss is predicted only in the peri-prosthetic region. The second design is far more likely to cause implant failure. Yet, the model favours it over the first.

Another commonly-used bone loss prediction function is called ‘‘Stress Shielding Increase’’ (SSI) [29,61]. In this model, the von Mises stresses are computed before and after THA. SSI is defined as the relative difference between the two, averaged over a specified region.

$$SSI = \frac{\langle \sigma_{VMS}^{pre-THA} \rangle - \langle \sigma_{VMS}^{THA} \rangle}{\langle \sigma_{VMS}^{pre-THA} \rangle} \quad (5)$$

where $\sigma_{VMS}^{pre-THA}$ and σ_{VMS}^{THA} are the von Mises stresses in the femur before and after THA and

$$\begin{aligned} \langle \sigma_{VMS}^{pre-THA} \rangle &= \frac{1}{\sum_e V^e} \sum_e \int_{V^e} (\sigma_{VMS}^{pre-THA})^e dV \\ \langle \sigma_{VMS}^{THA} \rangle &= \frac{1}{\sum_e V^e} \sum_e \int_{V^e} (\sigma_{VMS}^{THA})^e dV \end{aligned} \quad (6)$$

are the averages of the stress over a set of elements. This formulation outputs performance values for each element set. However, it is unclear how a single overall performance value would be defined for use in an optimization setting. Furthermore, the choice of domain segmentation would likely affect results. In the extreme, with a single domain, the function loses all local information. On the other hand, in the case of single-element domains, the function becomes highly susceptible to finite-element-related instabilities and numerical rounding errors, especially in cases where stress values approach zero.

In addition to the above-mentioned issues, both formulations ignore the effects of local stress over-loading. Over-loading can induce bone formation which alters the stress distribution along the bone-implant interface, potentially destabilizing the implant. Moreover, severe over-stressing can cause stress fractures which can cause chronic pain and generally weaken the bone-implant system [62,63].

In this work, we present an alternative function which aims to address the above-mentioned issues. This approach takes into account both bone resorption and bone apposition, as well as their relative magnitudes. In this way, the algorithm aims to minimize all bone remodelling, and prioritizes areas in which greater remodelling is predicted.

The well-established bone remodelling algorithm, proposed by Huiskes and Weinans, defines the predicted change in bone density in a given time step as a piece-wise function based on the local strain energy density [64]. For values below a certain threshold, bone loss is predicted, and for values above the threshold, bone apposition is predicted. Additionally, a stable region is defined, for which no net remodelling is predicted. Formally stated, the bone remodelling $\frac{\partial \rho}{\partial t}$ in time step t is defined as:

$$\frac{\partial \rho}{\partial t} = \begin{cases} C_1(\Xi_t - k(1+s))^m & k(1+s) < \Xi_t \\ 0 & k(1-s) \leq \Xi_t \leq k(1+s) \\ -C_2(k(1-s) - \Xi_t)^n & \Xi_t < k(1-s) \end{cases} \quad (7)$$

where Ξ is the local strain energy density, k is the stable strain energy density, often chosen as the original pre-THA value, s is a threshold defining the stable zone, C_1 , C_2 , m and n are constant tuning parameters. In practice,

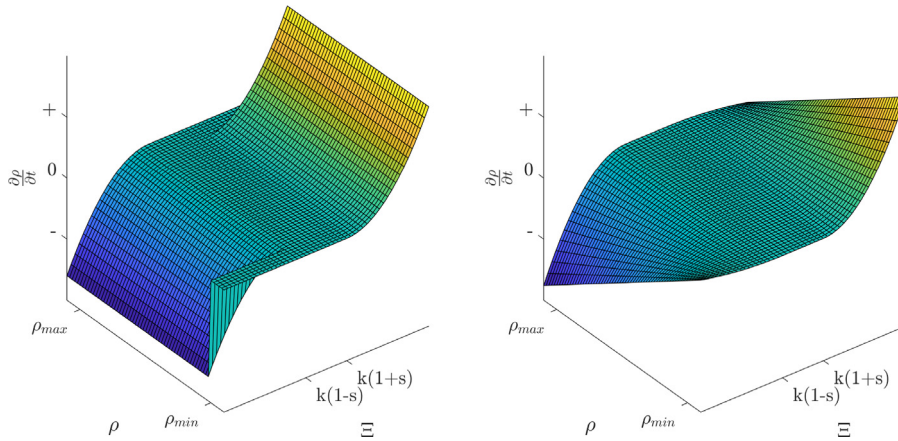


Fig. 8. Original (left) and augmented (right) Huijkes bone remodelling algorithms described in Eqs. (7) and (8).

normalized densities are constrained to values between $[\rho^{min} \rho^{max}]$. This introduces discontinuities, as shown in Fig. 8 (left). As a result, the function is non-differentiable along the density extrema, which can cause convergence problems in a gradient-based optimization routine. To remedy this issue, a minor modification is proposed:

$$\frac{\partial \rho}{\partial t} = \begin{cases} C_1(\rho^{max} - \rho_t) \cdot (\Xi_t - k(1 + s))^m & k(1 + s) < \Xi_t \\ 0 & k(1 - s) \leq \Xi_t \leq k(1 + s) \\ -C_2(\rho_t - \rho^{min}) \cdot (k(1 - s) - \Xi_t)^n & \Xi_t < k(1 - s) \end{cases} \quad (8)$$

The added factors $(\rho^{max} - \rho_t)$ and $(\rho_t - \rho^{min})$ smoothly constrain the density ρ_t to specified maximum and minimum values ρ^{max} and ρ^{min} , thereby eliminating the discontinuities, without affecting the general behaviour of the model. In this work, the following constant values were used: $k = \Xi_{unresected}$, $s = 0$, $C_1 = 10^{-2}$, $C_2 = 1$, $m = n = 1$, $\rho^{min} = 0.1$, $\rho^{max} = 1$.

The bone remodelling objective is defined as the sum of the unsigned changes in bone density throughout the bone, in the first iteration:

$$F_r = \int_V \left| \frac{\partial \rho}{\partial t} \right|_{t=0} dV \quad (9)$$

where V is the bone domain. We note that in the tuning parameters C_1 , C_2 , m and n , which were originally intended to ensure accuracy in the bone remodelling simulation, can instead be used to prioritize bone resorption over bone apposition, if desired. This formulation, provides a robust and flexible way to evaluate and optimize performance in terms of bone remodelling.

2.4. Interface fracture risk

The second failure mechanism considered in this work is interface fracture due to inappropriate stress conditions along the bone-implant interface. In cementless THA, no adhesive material is used to fixate the implant. Instead, press-fitting and eventual bone ingrowth stabilize the implant. In this context, inappropriate stress conditions can impede bone ingrowth and create wear particles by inducing micro-motions along the interface. Prior works have demonstrated that when the interface fails, fracture tends to occur within the brittle bone tissue [65,66]. It is therefore appropriate to estimate the risk of failure via an orthotropic brittle material model such as the Tsai–Wu failure criterion or the elliptic multi-axial Hoffman failure criterion (HFC) [67]. This latter model defines the local failure risk as an elliptic function of the normal stress σ and shear stress τ :

$$f_H(\sigma, \tau) = \frac{1}{S_t S_c} \sigma^2 + \left(\frac{1}{S_t} - \frac{1}{S_c} \right) \sigma + \frac{1}{S_s^2} \tau^2 \quad (10)$$

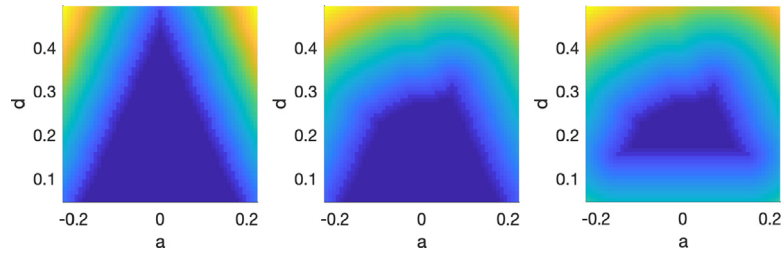


Fig. 9. Distance fields corresponding to the design spaces shown in Fig. 4.

where S_t , S_c , and S_s are the local strengths of the material in tension, compression and shear loading, respectively. These strengths are defined as a function of local material density, according to a power law.

$$S_x = a_x \cdot \rho^b \tag{11}$$

Here, $a_t = 2.63$, $a_c = 8.29$, $a_s = 6.60$, and $b = 1.65$ [68].

The global interface risk function is defined as the p-norm of local risk measured over the interface. For lower p values, the function approaches the set mean, whereas for high p values, the function approaches the set maximum. In this work, $p = 12$.

$$F_\sigma = \|\{f_H(\sigma, \tau)\}\|_p \tag{12}$$

2.5. Multi-objective optimization

In this section, we formulate a multi-objective optimization problem in which the goal is to find an implant design which simultaneously minimizes the bone remodelling and interface fracture risk functions. The implant is assumed to be a quasi-periodic arrangement of cubic anti-chiral unit cells, the geometric parameters for which will serve as design variables.

The two objectives are aggregated into a single global objective via linear scalarization.

$$F = w_\sigma \cdot F_\sigma + w_r \cdot F_r \tag{13}$$

where w_σ and w_r are weighting factors. In this work, the weights are chosen such that the weighted components of the objective are equal prior to the optimization. This helps avoid scaling issues, in which the objective with largest magnitude is favoured by the optimization method, to the detriment of the other. Furthermore, constraints are added to ensure that the interface stress F_σ and bone remodelling F_r objectives are below prescribed critical values F_r^* and F_σ^* , respectively.

2.5.1. Design space

In order to ensure that the geometric parameter combinations for each element belong to the permitted design space as described in Section 2.1, a signed distance field is generated from the binary design space (Fig. 9). The distance field, computed via a distance transform, maps the distance from any point $x \in \Omega$ to the boundary of a domain $\Phi \subseteq \Omega$. Points outside of Φ correspond to positive values, and points within Φ are assigned a value of 0. The sum of the distance field is included as a constraint in the optimization routine.

Formally, the element-wise constraint C_i with design element i is

$$C_i = DT_\Phi(a_i, d_i) \tag{14}$$

where Φ is a binary representation of the permissible parameter combinations, and $DT_\Phi(a_i, d_i)$ is the distance transform of Φ , evaluated at (a_i, d_i) . The sum of the element-wise constraint values for all n elements is then constrained to be less than or equal to zero.

$$\sum_{i=1}^n C_i \leq 0 \tag{15}$$

2.5.2. Optimization formulation

To ensure that the optimized implant is not unduly sensitive to variations in the loading conditions, we consider multiple loading conditions: walking and stair climbing. We formulate our design objective as a min-max problem in which the worst case performance is optimized. Overall, the optimization problem is

$$\begin{aligned}
 \min_{\mathbf{a}, \mathbf{d}} \quad & \max_{l \in L} (w_\sigma \cdot F_\sigma^l + w_r \cdot F_r^l) \\
 \text{subject to} \quad & \mathbf{K}\mathbf{U}_l = \mathbf{F}_l \quad l = 1, \dots, L \\
 & F_r^l \leq F_r^{l*} \quad l = 1, \dots, L \\
 & F_\sigma^l \leq F_\sigma^{l*} \quad l = 1, \dots, L \\
 & \sum_{i=1}^n C_i \leq 0
 \end{aligned} \tag{16}$$

where F_σ^l and F_r^l are the interface stress and bone remodelling objectives for load case l , and L is the number of the load cases considered. The state equation $\mathbf{K}\mathbf{U}_l = \mathbf{F}_l$ is solved to obtain the unknown displacements \mathbf{U}_l corresponding to load \mathbf{F}_l . Additional constraints ensure that the bone remodelling F_r^l and interface stress F_σ^l objectives are below the prescribed critical values F_r^{l*} and F_σ^{l*} , respectively. The stress tensors σ_e are computed for each element e as:

$$\sigma_e^l = \mathbf{C}_e \mathbf{B}_e \mathbf{u}_e^l \tag{17}$$

where \mathbf{C}_e is the local isotropic constitutive tensor, with $\nu = 0.3$ and E is defined as a function of the local bone density, according to [69]:

$$E(\rho) = \begin{cases} 1.904 \rho^{1.64} & 0 < \rho < 0.95 \\ 2.065 \rho^{3.09} & 0.95 \leq \rho \leq 1 \end{cases} \tag{18}$$

\mathbf{B}_e is the strain-displacement matrix and \mathbf{u}_e^l is the solution corresponding to the degrees of freedom associated with element e .

To obtain the local Hoffman interface failure risk, the stress tensors are aligned to the interface normal direction via the coordinate transformation, i.e.,

$$(\sigma_e^l)_{\perp}^{full} = \mathbf{Q}(\mathbf{n}_e) \cdot (\sigma_e^l)^{full} \cdot \mathbf{Q}(\mathbf{n}_e)^T \tag{19}$$

Here, \mathbf{n}_e is the interface normal, $\mathbf{Q}(\mathbf{n}_e)$ is a coordinate transformation matrix, and $(\sigma_e^l)^{full}$ and $(\sigma_e^l)_{\perp}^{full}$ are the full rank element stress tensors. The normal σ and shear τ components are obtained from the components of $(\sigma_e^l)_{\perp}^{full}$.

The normal and shear stress components σ_e and τ_e are obtained from the interface-aligned stress tensor that are computed as $(\sigma_e^l)_{\perp}^{full}(1, 1)$ and $\sqrt{(\sigma_e^l)_{\perp}^{full}(1, 2)^2 + (\sigma_e^l)_{\perp}^{full}(1, 3)^2}$, respectively.

Finally, since we are concerned with elements along the bone-implant interface, we eliminate the distant elements by dividing the element-wise Hoffman function $f(\sigma_e)$ by the distance from the centroid of the element to the implant boundary,

$$\tilde{f}(\sigma_e) = \frac{f(\sigma_e)}{d(x_e)}. \tag{20}$$

For elements that intersect with the implant boundary, $d(x_e)$ is the distance from the centroid of the portion of the element which lies within the implant. The global risk function is then given by:

$$F_\sigma = \left(\sum_{e \in \mathbb{N}} \tilde{f}(\sigma_e)^p \right)^{\frac{1}{p}} \tag{21}$$

2.5.3. Filtering

The proposed optimization strategy is susceptible to mathematical instabilities, introduced by the finite element representation. A common solution is to regularize the design variables by means of a convolutional operator. Specifically, the convolutional operator calculates a weighted average of the neighbouring values via

$$\tilde{\phi}_e = \frac{\sum_{i \in \mathbb{M}} w_{i,e} \phi_i}{\sum_{i \in \mathbb{M}} w_{i,e}}, \tag{22}$$

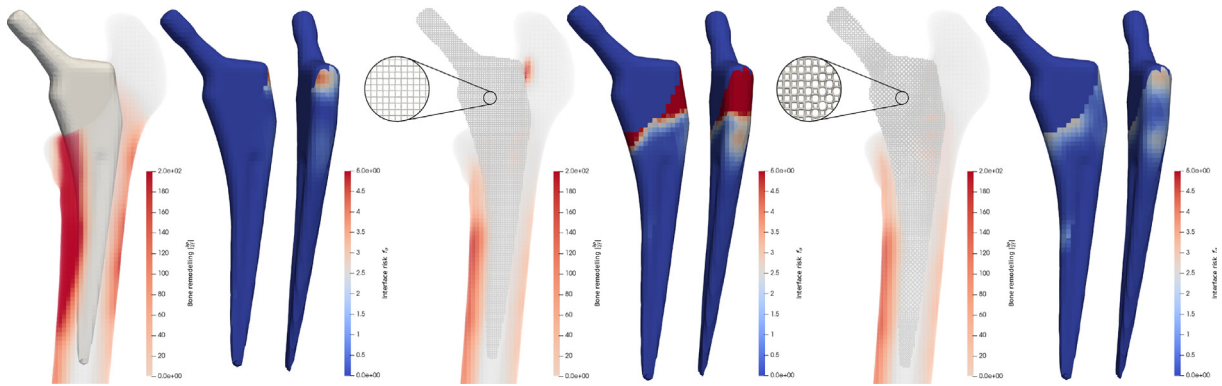


Fig. 10. The design and performance of (a) solid, (b) uniform lattice, (c) optimized heterogeneous lattice titanium implants in terms of local bone remodelling and the Hoffman interface stress risk indices.

where ϕ refers to design variables a and d . \mathbb{M}_e is the set of voxels close to voxel e , i.e.,

$$\mathbb{M}_e = \{i \mid \|x_i - x_e\|_2 \leq r_e\} \quad (23)$$

with filter radius r_e . The weighting factor $w_{i,e}$ is inversely related the distance between voxels i and e , i.e.,

$$w_{i,e} = 1 - \frac{\|x_i - x_e\|_2}{r_e} \quad (24)$$

2.5.4. Sensitivity analysis

The optimization problem is solved using the method of moving asymptotes (MMA) [41], which takes in the sensitivities of the objective and constraints with respect to the design variables. These sensitivities are obtained via adjoint analysis. For details, refer to [Appendix](#).

3. Results & discussion

In this section, the proposed optimization strategy is applied to the design of a hip stem. The implant is made from titanium ($E = 116$ GPa, $\nu = 0.34$), and its geometry is based on a standard tapered, press-fitted design, described in [70]. The loading conditions are based on the walking and stair climbing profiles described in [58]. The optimized design's performance is compared to those of a fully solid and highly porous ($E = 3.4$ GPa, $\nu = 0.05$, $\mu = 0.06$ GPa) titanium designs. The accuracy of the homogenization-based finite element analysis (FEA) is verified, in 2D, by re-evaluating the bone-implant system in full micro-architectural detail. Finally, we investigate the performance of the algorithm for various implant geometries.

An optimized hip stem is shown in [Fig. 10](#), alongside benchmark solid and porous designs. As expected, the solid implant exhibits significant bone remodelling due to the stress shielding, but presents a low risk of interface fracture. On the other hand, the compliant porous design generates considerably lower bone resorption, but induces a high risk of interface fracture in the proximal lateral interface region. By contrast, the optimized design generates 21.2% less bone resorption than the porous implant, and 13.2% less interface stress than the solid implant. Moreover, the predicted bone remodelling associated with the optimized design is 64.0% lower than that of the conventional solid implant. Improved performance in terms of both metrics, compared to the benchmark solid and porous designs, is achieved by setting the objective constraints according to the performance of the benchmarks. If the constraints are respected, this guarantees that the optimized design shall perform at least as well as the benchmark designs, in terms of their respective strengths. Performance in terms of the interface fracture risk and bone remodelling objectives is computed according to Eqs. (21) and (9), respectively, and presented in [Table 1](#). Performance in terms of the bone resorption metric proposed by Huiskes [64] is also included, for comparison.

The optimization history, shown in [Fig. 11](#), highlights the stability of the optimization routine. The initial, uniform lattice ([Fig. 10-b](#)) converges smoothly to the final design ([Fig. 10-c](#)) after 50 iterations. The interface risk and bone remodelling objectives are each normalized with respect to their initial values (iteration 1). In this case, the interface

Table 1

Performance results for all studied implant configurations. Interface risk, bone remodelling, and Huiskes bone resorption function are computed according to Eqs. (21), (9), and (4), respectively.

| Shape | Microarchitecture | Fig. | FEA | Interface risk (F_σ) | Bone remodelling (F_r) | Huiskes bone resorption |
|-----------------------|---|------|---------|-------------------------------|----------------------------|-------------------------|
| Type 1 (Single-wedge) | Solid | 10 | 3D/AH | 5.85×10^0 | 2.67×10^8 | 33.5% |
| | 30% density cubic lattice | 10 | 3D/AH | 5.18×10^2 | 1.22×10^8 | 17.8% |
| | Optimized CAC lattice | 10 | 3D/AH | 5.08×10^0 | 9.61×10^7 | 16.1% |
| | Optimized CAC lattice under manufacturing constraints | 15 | 3D/AH | 6.07×10^0 | 1.11×10^8 | 17.2% |
| Type 2 (Double-wedge) | Solid | 14 | 3D/AH | 3.96×10^0 | 2.75×10^8 | 29.9% |
| | 30% density cubic lattice | 14 | 3D/AH | 2.27×10^3 | 4.07×10^8 | 14.3% |
| | Optimized CAC lattice | 14 | 3D/AH | 1.34×10^1 | 1.08×10^8 | 17.8% |
| Type 3 (Tapered) | Solid | 14 | 3D/AH | 7.5×10^0 | 2.75×10^8 | 30.1% |
| | 30% density cubic lattice | 14 | 3D/AH | 3.49×10^3 | 8.55×10^8 | 13.6% |
| | Optimized CAC lattice | 14 | 3D/AH | 1.91×10^1 | 1.24×10^8 | 19.4% |
| Type 1-Short | Solid | 14 | 3D/AH | 5.84×10^0 | 2.08×10^8 | 17.3% |
| | 30% density cubic lattice | 14 | 3D/AH | 3.87×10^2 | 1.01×10^8 | 8.32% |
| | Optimized CAC lattice | 14 | 3D/AH | 4.91×10^0 | 8.92×10^7 | 8.97% |
| Type 1 (Single-wedge) | Optimized CAC lattice | 13 | 2D/AH | 7.93×10^0 | 3.36×10^{10} | NA |
| | Optimized CAC lattice | 13 | 2D/Full | 8.66×10^0 | 3.83×10^{10} | NA |

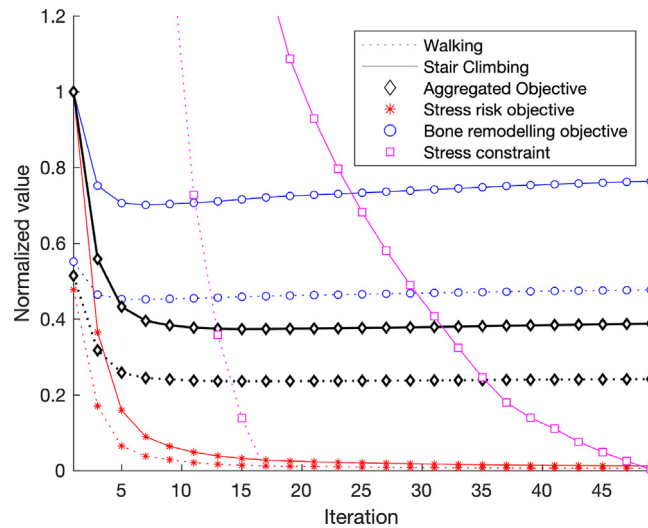


Fig. 11. The optimization history starting from the uniform lattice shown in Fig. 10-b and ending in the design shown in Fig. 10-c.

stress risk was constrained to be less than or equal to that of the solid implant design. As a result, the interface stress is prioritized over bone remodelling, if both objectives cannot be improved simultaneously.

The optimized implant possesses a highly non-uniform geometric parameter distribution, spanning nearly the entire range of allowed parameter combinations (Fig. 12). This heterogeneity is precisely what enables its improved performance. This was confirmed by running the optimization routine with a reduced design space.

The proposed optimization routine, like other multi-scale finite element-based methods, relies on asymptotic homogenization. This means that the fine scale mechanics are not captured in their true detail. While it has been demonstrated that AH is accurate for semi-periodic structures with large length scale separation [71], we confirm the reliability of our model by comparing the AH-based performance with that of the full-detail structure. Simplification to 2D was necessary to reduce the computational cost of the analysis. Additionally, a relatively coarse ground mesh with elements of the size 2×2 mm was used for the AH-based study, such that each unit cell of the micro-architected

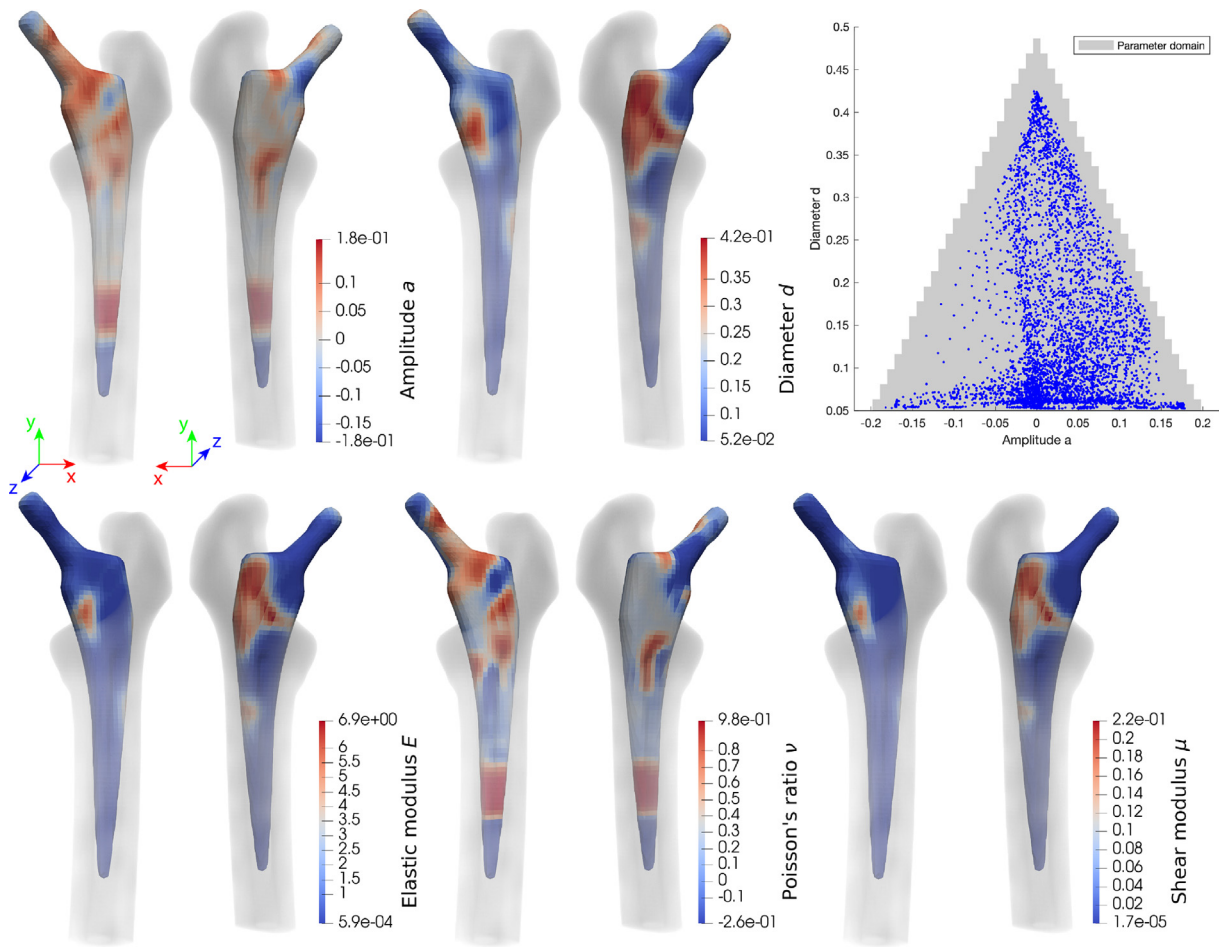


Fig. 12. Geometric parameter (top) and mechanical property (bottom) distribution associated with the implant shown in Fig. 10-c.

implant was modelled as 60×60 standard linear quadrilateral finite elements in the detailed study (~ 2.7 million $33 \times 33 \mu\text{m}$ elements). The results indicate that the homogenization-based model is highly accurate, both in terms of bone remodelling and interface fracture risk, with 8.4% difference in the peak interface risk predictions and 14.0% difference in total bone remodelling. AH-based and FEA considering the full micro-architectural detail are shown in Fig. 13. Note that the FEA study considering full detail uses a 5 times finer mesh in the bone region in order to capture any stress concentrations introduced by the sharp edges of the implant micro-architecture. This explains small discrepancies and the oscillation of the fracture risk along the interface.

3.1. Alternative implant shapes

The results presented in this work make use of a common implant geometry. However, many implant designs exist in the industry. In particular, minimally invasive implants with shortened stems have recently been gaining traction [72]. It is therefore relevant to assess the performance of the proposed optimization strategy with various implant geometries. To this end, three alternative implant designs were studied, namely Type 2, Type 3, and Type 1-short stems, according to the Mont group classification system [73].

In Fig. 14, three alternative implant geometries are optimized. The results indicate that the optimization routine is able to significantly improve performance, in each case. In all cases, the solid implant (left) triggers high remodelling, particularly along the medial interface. The interface fracture risk is low in each case, with maximal values near the resected surface, especially along the lateral interface. The uniform highly porous lattice (centre)

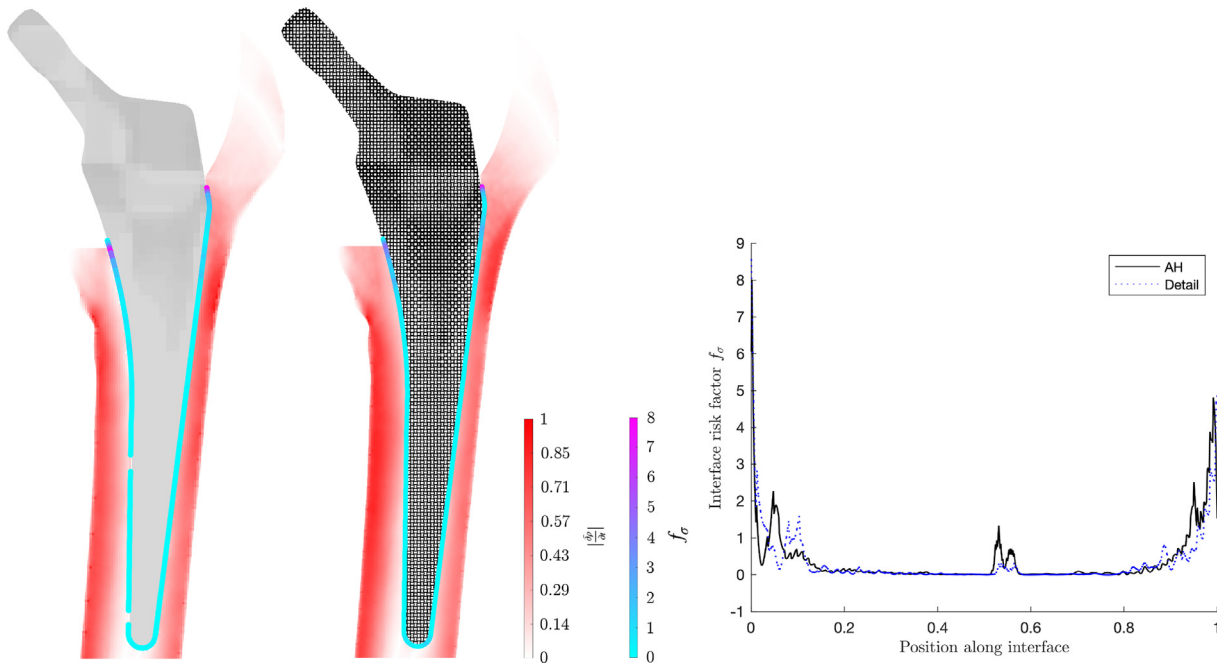


Fig. 13. Performance comparison of asymptotic homogenization-based FEA (left) and FEA considering full micro-architectural detail (right). The homogenization-based implant design is shown here in terms of mean local density.

triggers less bone remodelling along the bone shaft, but introduces apposition in the greater trochanter, due to the increased stress in this region. This increased stress also introduces a significant risk of interface fracture in this area and in the interface near resected bone surface. The optimized lattice implants (right) induce an intermediate risk of interface fracture, comparable to (Type 1-short) or somewhat greater (Type 2 and Type 3) than their solid implant counterparts. Bone remodelling is of the same order as for the uniform lattice design, with slightly worse performance along the bone shaft and better performance in the greater trochanter. The performances are summarized in Table 1. In all studies, the optimization procedure produces a design with considerably less bone remodelling and lower interface risk than the uniform lattice, however, we notice that in some cases (Type 2, Type 3, and Type 1 under manufacturing constraints), the interface risk is somewhat worse than in the solid design. This is likely due to the constraints on the design space that prevent any part of the design from becoming fully solid.

3.2. Manufacturing constraints

The results presented thus far are dependent upon manufacturing methods which are not yet reliable and cost-competitive with standard implant designs. In order to ensure the accuracy of the homogenization method employed in this work, 5 micro-architecture unit cells per centimetre were used, together with linear filtering of the design variables according to Eq. (22) with $r_e = 3.2$. With a minimum diameter setting of 0.05, the minimum feature size is 100 μm , which corresponds to the accuracy limit of the current generation of SLM machines [74]. While SLM technology is still improving, we demonstrate the effectiveness of our method for use with readily available machines by constraining the minimum feature size, for both material and gaps to 200 μm . The results presented in Fig. 15 and Table 1 indicate that, even with a significant reduction to the design space, bone remodelling can be reduced by 58.4% as compared to a solid implant, with a negligible impact on the risk of interface fracture.

4. Conclusion

The optimization strategy presented in this work has proven capable of simultaneously reducing the risk of interface fracture as well as bone remodelling (and resorption), in-silico. The proposed method incorporates an accurate and versatile bone remodelling function and an efficient decoupled multi-scale strategy, capable of accurately

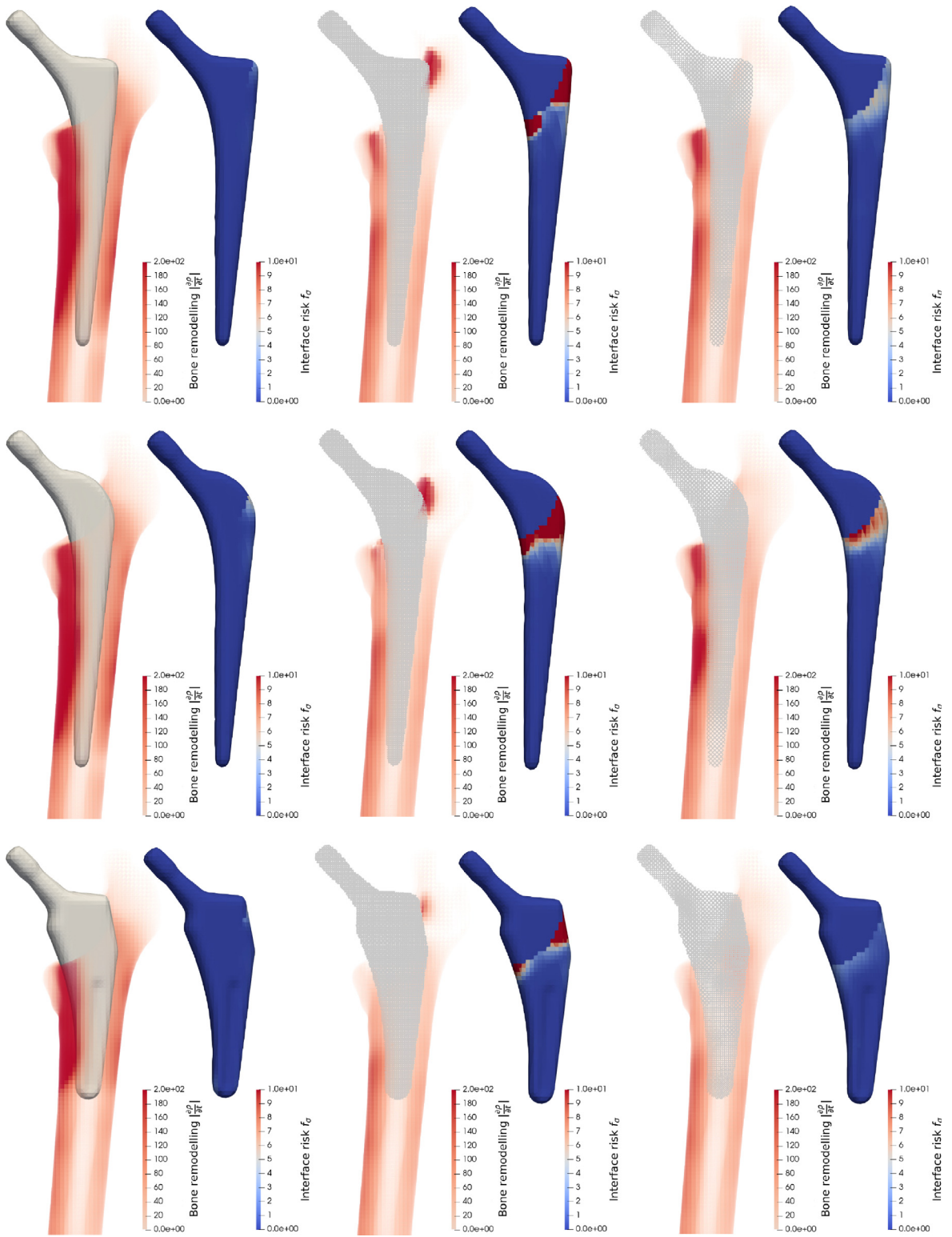


Fig. 14. Performance comparison between solid (left column), uniform lattice (centre column), and optimized lattice (right column) for Type 2 (top row), Type 3 (middle row), and Type 1-short (bottom row) implant geometries (Mont classification).

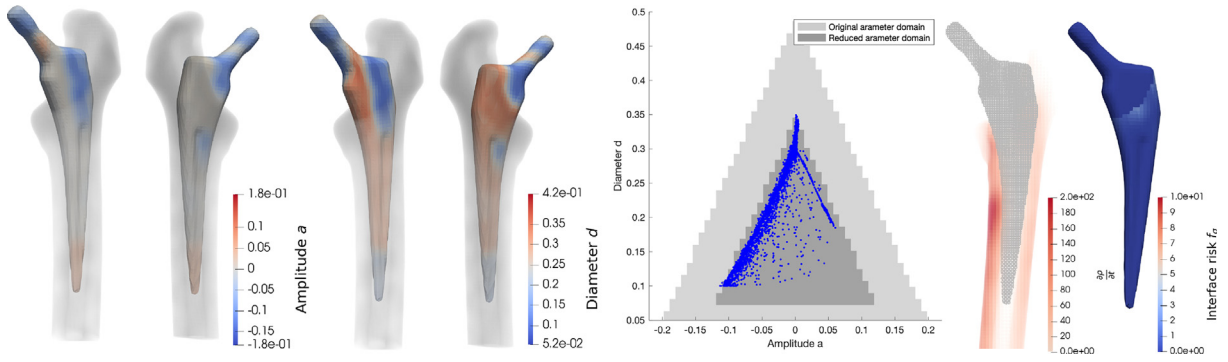


Fig. 15. The design and performance of an optimized implant with a length scale of 200 μm . The performance values are included in Table 1.

capturing interface mechanics at comparatively low computational cost. Additionally, a generalized cubic anti-chiral parametric micro-architecture, highly suited to functionally graded structural design and capable of achieving a wide range of mechanical properties was presented. Along side this, a new method to incorporate geometric constraints on the parametric design space allows for the inclusion of any number of micro-level constraints, such as minimum/maximum length scale (feature size), porosity, pore size, etc., at zero extra computational cost.

This work was limited to computer simulation and should be followed up with physical testing, both in vitro and in vivo. Moreover, these results are based on linear finite element analyses, which do not capture micro-scale behaviour and non-linear effects such as buckling. While the incorporation of non-linear analysis in the proposed methodology is computationally infeasible, a non-linear analysis of the final design on a high performance cluster should be performed.

Declaration of competing interest

The authors declare that they have no known competing financial interests or personal relationships that could have appeared to influence the work reported in this paper.

Acknowledgement

This work is part of the research program: “Metallic clay: shape-matching orthopaedic implants” with project number 16582, which is financed by the Dutch Research Council (NWO), Netherlands.

Appendix

Sensitivity analysis

In gradient-based optimization, the sensitivity of the objectives and constraints with respect to the design variables is required. In this work, both the bone remodelling and interface fracture risk objective functions sensitivity with respect to a generic design variable ϕ_i are computed via chain rule:

$$\frac{\partial F_x}{\partial \phi_e} = \sum_{i \in \mathbb{M}} \left(\frac{\partial F_x}{\partial \tilde{\phi}_i} \frac{\partial \tilde{\phi}_i}{\partial \phi_e} \right) \tag{25}$$

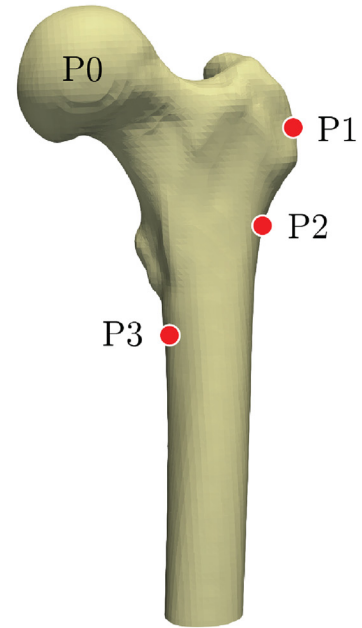
where F_x is either the remodelling function F_r or the interface fracture objective F_σ and $\tilde{\phi}_i$ is the filtered design variable ϕ_i

The sensitivity of the objective with respect to the filtered design variable $\tilde{\phi}_i$ is obtained via an adjoint analysis

$$\frac{\partial F_x}{\partial \phi_i} = -\lambda_i^x \frac{\partial \mathbf{k}_i}{\partial \phi_i} \mathbf{u}_i \tag{26}$$

| Load case: Walking (BW = 836N) | | | | |
|------------------------------------|-------|-------|--------|-------|
| Force | x | y | z | Locus |
| hip contact | -54.0 | -32.8 | -229.2 | P0 |
| intersegmental resultant | -8.1 | -12.8 | -78.2 | P0 |
| abductor | 58.0 | 4.3 | 86.5 | P1 |
| tensor fascia latae, proximal part | 7.2 | 11.6 | 13.2 | P1 |
| tensor fascia latae, distal part | -0.5 | -0.7 | -19.0 | P1 |
| vastus lateralis | -0.9 | 18.5 | -92.9 | P2 |

| Load case: Stair Climbing (BW = 847N) | | | | |
|--|-------|-------|--------|-------|
| Force | x | y | z | Locus |
| hip contact | -59.3 | -60.6 | -236.3 | P0 |
| intersegmental resultant | -13.0 | -28.0 | -70.1 | P0 |
| abductor | 70.1 | 28.8 | 84.9 | P1 |
| ilio-tibial tract, proximal part _{cc} | 10.5 | 3.0 | 12.8 | P1 |
| ilio-tibial tract, distal part | -0.5 | -0.8 | -16.8 | P1 |
| tensor fascia latae, proximal part | 3.1 | 4.9 | 2.9 | P1 |
| tensor fascia latae, distal part | -0.2 | -0.3 | -6.5 | P1 |
| vastus lateralis | -2.2 | 22.4 | -135.1 | P2 |
| vastus medialis | -8.8 | 39.6 | -267.1 | P3 |



| Coordinates | | | |
|-------------|--------|--------|---------|
| Point | x | y | z |
| P0 | 0.00 | 0.00 | 0.00 |
| P1 | -67.83 | -11.90 | -35.00 |
| P2 | -49.40 | -5.01 | -78.20 |
| P3 | -18.79 | 8.82 | -106.23 |

Fig. 16. Load profiles used in the finite element analysis, obtained from [58]. The forces (in percentage of body weight), and the coordinates (in millimetres) are given in a local coordinate system of the femur [75]. The hip contact force acts at the origin of the coordinate system labelled as P0. The attachments or wrapping points of the muscles are labelled P1 to P3.

where \mathbf{u}_i are the displacements of the DOFs corresponding to element i , $\frac{\partial \mathbf{k}_i}{\partial \phi_i}$ is the sensitivity of the element stiffness matrix with respect to the design variable, and the vector λ_i contains the i 'th element's DOFs of the adjoint vector. The adjoint field λ^x is the solution of the adjoint problem:

$$\mathbf{K}\lambda^x = \frac{\partial F_x}{\partial \mathbf{u}} \tag{27}$$

where the right hand side is obtained through the finite element assembly of the element contributions of, in the case of the bone remodelling objective

$$\frac{\partial F_r}{\partial \mathbf{u}_i} = \frac{2 \operatorname{sign}(\frac{\partial \rho_i}{\partial t})}{\rho_i} \frac{\partial(\frac{\partial \rho_i}{\partial t})}{\partial \Xi_i} \mathbf{u}_i^T \mathbf{k}_i \tag{28}$$

and in the case of the interface fracture risk objective,

$$\frac{F_\sigma}{\partial \sigma_e} = \sum_{i \in \mathbb{M}} \frac{\left(\sum \tilde{f}(\sigma_i, \tau_i)^p\right)^{\frac{1}{p}-1}}{d(x_e)} \frac{\partial \tilde{f}(\sigma_i, \tau_i)}{\partial f(\sigma_e, \tau_e)} \frac{\partial \tilde{f}(\sigma_i, \tau_i)}{\partial \sigma_i} \tag{29}$$

$$\frac{\partial \tilde{f}(\sigma_i, \tau_i)}{\partial \sigma_i} = \left(\frac{2}{S_t S_c} \sigma_i + \left(\frac{1}{S_t} + \frac{1}{S_c} \right) \right) \frac{\partial \sigma_i}{\partial \sigma_i} + \frac{2}{S_s^2} \tau_i \frac{\partial \tau_i}{\partial \sigma_i} \quad (30)$$

where

$$\frac{\partial \sigma_i}{\partial \sigma_i} = e_{11} \quad (31)$$

with e_{11} defined as a 3×3 matrix of zeros with 1 at position (1, 1). Similarly,

$$\frac{\partial \tau_i}{\partial \sigma_i} = \frac{1}{2\sqrt{\tau_i}} \begin{bmatrix} 0 & \sigma_{12}^i & \sigma_{13}^i \\ \sigma_{21}^i & 0 & 0 \\ \sigma_{31}^i & 0 & 0 \end{bmatrix} \quad (32)$$

where σ_{jk}^i is the component of the full rank stress tensor at position (j, k) . Finally, the sensitivities of the stress tensor with respect to the element DOF displacements is

$$\frac{\partial \sigma_i}{\partial \mathbf{u}_i} = \mathbf{Q}(\mathbf{n}_e)(\mathbf{C}_i \mathbf{B}_i)^{full} \mathbf{Q}^T(\mathbf{n}_e) \quad (33)$$

Loads and boundary conditions

In this work, the proximal part of the femur is modelled in isolation, with the sectioned distal face fully constrained and a set of static loads applied over 1 cm^3 regions. Load cases for walking and stair climbing, presented in Fig. 16, were retrieved from [58], with slight modification to the load application points to fit the bone model.

References

- [1] M. Ridzwan, S. Shuib, A. Hassan, A. Ahmed Shokri, M. Ibrahim, Problem of stress shielding and improvement to the hip implant designs: A review, *J. Med. Sci.* 7 (3) (2007) 460–467, <http://dx.doi.org/10.3923/jms.2007.460.467>.
- [2] S. Kurtz, F. Mowat, K. Ong, N. Chan, E. Lau, M. Halpern, Prevalence of primary and revision total hip and knee arthroplasty in the United States from 1990 through 2002, *J. Bone Joint Surg.* 87 (7) (2005) 1487–1497, <http://dx.doi.org/10.2106/JBJS.D.02441>.
- [3] R. Pivec, A. Johnson, S. Mears, M. Mont, Hip arthroplasty, *Lancet* 380 (9855) (2012) 1768–1777, [http://dx.doi.org/10.1016/S0140-6736\(12\)60607-2](http://dx.doi.org/10.1016/S0140-6736(12)60607-2).
- [4] P. Kowalczyk, Design optimization of cementless femoral hip prostheses using finite element analysis, *J. Biomech. Eng.* 123 (5) (2001) 396–402, <http://dx.doi.org/10.1115/1.1392311>.
- [5] F.F. Buechel, M.J. Pappas, Properties of materials used in orthopaedic implant systems, in: *Principles of Human Joint Replacement*, Springer, 2015, pp. 1–32, http://dx.doi.org/10.1007/978-3-319-15311-7_1.
- [6] E.F. Morgan, G.U. Unnikrisnan, A.I. Hussein, Bone mechanical properties in healthy and diseased states, *Annu. Rev. Biomed. Eng.* 20 (2018) 119–143, <http://dx.doi.org/10.1146/annurev-bioeng-062117-121139>.
- [7] P. Hill, Bone remodelling, *Br. J. Orthod.* 25 (2) (1998) 101–107, <http://dx.doi.org/10.1093/ortho.25.2.101>.
- [8] R. Crowninshield, R. Brand, R. Johnston, J. Milroy, An analysis of femoral component stem design in total hip arthroplasty, *J. Bone Joint Surg.* 62 (1) (1980) 68–78, URL <http://europepmc.org/abstract/MED/7351419>.
- [9] A. Rohlmann, U. Mössner, G. Bergmann, G. Hees, R. Kölbl, Effects of stem design and material properties on stresses in hip endoprostheses, *J. Biomed. Eng.* 9 (1) (1987) 77–83, [http://dx.doi.org/10.1016/0141-5425\(87\)90104-X](http://dx.doi.org/10.1016/0141-5425(87)90104-X).
- [10] B.-A. Behrens, C. Wirth, H. Windhagen, I. Nolte, A. Meyer-Lindenberg, A. Bouguecha, Numerical investigations of stress shielding in total hip prostheses, *Proc. Inst. Mech. Eng. H* 222 (5) (2008) 593–600, <http://dx.doi.org/10.1243/09544119JEIM139>.
- [11] W.D. Bugbee, W.J. Culpepper, C.A. Engh, C.A. Engh, Long-term clinical consequences of stress-shielding after total hip arthroplasty without cement, *J. Bone Joint Surg.* 79 (7) (1997) 1007–1012, <http://dx.doi.org/10.2106/00004623-199707000-00006>.
- [12] T. Niinimäki, J. Junila, P. Jalovaara, A proximal fixed anatomic femoral stem reduces stress shielding, *Int. Orthop.* 25 (2001) 85–88, <http://dx.doi.org/10.1007/s002640100241>.
- [13] T. Renkawitz, F.S. Santori, J. Grifka, C. Valverde, M.M. Morlock, I.D. Learmonth, A new short uncemented, proximally fixed anatomic femoral implant with a prominent lateral flare: design rationals and study design of an international clinical trial, *BMC Musculoskelet. Disord.* 9 (2008) 147, <http://dx.doi.org/10.1186/1471-2474-9-147>.
- [14] J. Schmidt, M. Hackenbroch, The cenos hollow stem in total hip arthroplasty: first experiences in a prospective study, *Arch. Orthop. Trauma Surg.* 113 (3) (1994) 117–120, <http://dx.doi.org/10.1007/BF00441616>.
- [15] S. Gross, E. Abel, A finite element analysis of hollow stemmed hip prostheses as a means of reducing stress shielding of the femur, *J. Biomech.* 34 (8) (2001) 995–1003, [http://dx.doi.org/10.1016/S0021-9290\(01\)00072-0](http://dx.doi.org/10.1016/S0021-9290(01)00072-0).
- [16] A. Glassman, J. Bobyn, M. Tanzer, New femoral designs: do they influence stress shielding? *Clin. Orthop. Relat. Res.* 453 (2006) 64–74, <http://dx.doi.org/10.1097/01.blo.0000246541.41951.20>.
- [17] R. Huiskes, H. Weinans, B. van Rietbergen, The relationship between stress shielding and bone resorption around total hip stems and the effects of flexible materials, *Clin. Orthop. Relat. Res.* 274 (1992) 124–134, URL.

- [18] J. Simões, A. Marques, Design of a composite hip femoral prosthesis, *Mater. Des.* 26 (2005) 391–401, <http://dx.doi.org/10.1016/j.matdes.2004.07.024>.
- [19] M.-S. Scholz, J. Blanchfield, L.D. Bloom, B. Coburn, M. Elkington, J. Fuller, M. Gilbert, S. Muflahi, M.F. Pernice, S. Rae, J. Trevarthen, S. White, P. Weaver, I. Bond, The use of composite materials in modern orthopaedic medicine and prosthetic devices: A review, *Compos. Sci. Technol.* 71 (2011) 1791–1803, <http://dx.doi.org/10.1016/j.compscitech.2011.08.017>.
- [20] C. Wen, Y. Yamada, K. Shimojima, Y. Chino, T. Asahina, M. Mabuchi, Processing and mechanical properties of autogenous titanium implant materials, *J. Mater. Sci. Mater. Med.* 13 (4) (2002) 397–401, <http://dx.doi.org/10.1023/A:1014344819558>.
- [21] F. Matassi, A. Botti, L. Sirleo, C. Carulli, M. Innocenti, Porous metal for orthopedics implants, *Clin. Cases Miner. Bone Metabol.* 10 (2) (2013) 111–115, URL <https://europepmc.org/articles/PMC3796997>.
- [22] C.A. Engh, A.H. Glassman, K.E. Suthers, The case for porous-coated hip implants. The femoral side, *Clin. Orthop. Relat. Res.* (261) (1990) 63–81, URL <http://europepmc.org/abstract/MED/2245564>.
- [23] S. Evans, P. Gregson, Composite technology in load-bearing orthopaedic implants, *Biomaterials* 19 (15) (1998) 1329–1342, [http://dx.doi.org/10.1016/S0142-9612\(97\)00217-2](http://dx.doi.org/10.1016/S0142-9612(97)00217-2).
- [24] I. Catelas, J.J. Jacobs, Biologic activity of wear particles, *Instruct. Course Lect.* 59 (2010) 3–16, URL <http://europepmc.org/abstract/MED/20415362>.
- [25] J. Kuiper, H. Huiskes, Numerical optimization of hip-prosthetic stem material, in: J. Middleton, G. Pande, K. Williams (Eds.), *Recent Advances in Computer Methods in Biomechanics and Biomedical Engineering* Ams, Books and Journals International, 1992, pp. 76–84.
- [26] J. Kuiper, R. Huiskes, Mathematical optimization of elastic properties: application to cementless hip stem design, *J. Biomech. Eng.* 119 (2) (1997) 166–174, <http://dx.doi.org/10.1115/1.2796076>.
- [27] S. Arabnejad, D. Pasini, Multiscale design and multiobjective optimization of orthopedic hip implants with functionally graded cellular material, *J. Biomech. Eng.* 134 (2012) 031004, <http://dx.doi.org/10.1115/1.4006115>.
- [28] Y. He, D. Burkhalter, D. Durocher, J.M. Gilbert, Solid-lattice hip prosthesis design: Applying topology and lattice optimization to reduce stress shielding from hip implants, in: 2018 Design of Medical Devices Conference, ASME, 2018, http://dx.doi.org/10.1115/DMD2018-6804_V001T03A001.
- [29] M. Fraldi, L. Esposito, G. Perrella, A. Cutolo, S. Cowin, Topological optimization in hip prosthesis design, *Biomech. Model. Mechanobiol.* 9 (2010) 389–402, <http://dx.doi.org/10.1007/s10237-009-0183-0>.
- [30] Y. Wang, S. Arabnejad, M. Tanzer, D. Pasini, Hip implant design with three-dimensional porous architecture of optimized graded density, *J. Mech. Des.* 140 (11) (2018) 111406, <http://dx.doi.org/10.1115/1.4041208>.
- [31] S. Kashef, A. Asgari, T.B. Hilditch, W. Yan, V.K. Goel, P.D. Hodgson, Fracture toughness of titanium foams for medical applications, *Mater. Sci. Eng. A* 527 (29–30) (2010) 7689–7693, <http://dx.doi.org/10.1016/j.msea.2010.08.044>.
- [32] V.K. Balla, S. Bodhak, S. Bose, A. Bandyopadhyay, Porous tantalum structures for bone implants: fabrication, mechanical and in vitro biological properties, *Acta Biomater.* 6 (8) (2010) 3349–3359, <http://dx.doi.org/10.1016/j.actbio.2010.01.046>.
- [33] N. Taniguchi, S. Fujibayashi, M. Takemoto, K. Sasaki, B. Otsuki, T. Nakamura, T. Matsushita, T. Kokubo, S. Matsuda, Effect of pore size on bone ingrowth into porous titanium implants fabricated by additive manufacturing: an in vivo experiment, *Mater. Sci. Eng. C* 59 (2016) 690–701, <http://dx.doi.org/10.1016/j.msec.2015.10.069>.
- [34] O. Gauthier, J.-M. Boulter, E. Aguado, P. Pilet, G. Daculsi, Macroporous biphasic calcium phosphate ceramics: influence of macropore diameter and macroporosity percentage on bone ingrowth, *Biomaterials* 19 (1–3) (1998) 133–139, [http://dx.doi.org/10.1016/S0142-9612\(97\)00180-4](http://dx.doi.org/10.1016/S0142-9612(97)00180-4).
- [35] C.A. Engh, J. Bobyn, A.H. Glassman, Porous-coated hip replacement. The factors governing bone ingrowth, stress shielding, and clinical results, *J. Bone Joint Surg.* 69-B (1) (1987) 45–55, <http://dx.doi.org/10.1302/0301-620X.69B1.3818732>.
- [36] A. Reichardt, A.A. Shapiro, R. Otis, R.P. Dillon, J.P. Borgonia, B.W. McEnerney, P. Hosemann, A.M. Beese, Advances in additive manufacturing of metal-based functionally graded materials, *Int. Mater. Rev.* 66 (1) (2021) 1–29, <http://dx.doi.org/10.1080/09506608.2019.1709354>.
- [37] J. Parthasarathy, B. Starly, S. Raman, A. Christensen, Mechanical evaluation of porous titanium (Ti6Al4V) structures with electron beam melting (EBM), *J. Mech. Behav. Biomed. Mater.* 3 (3) (2010) 249–259, <http://dx.doi.org/10.1016/j.jmbbm.2009.10.006>.
- [38] R. Stamp, P. Fox, W. O’neill, E. Jones, C. Sutcliffe, The development of a scanning strategy for the manufacture of porous biomaterials by selective laser melting, *J. Mater. Sci. Mater. Med.* 20 (9) (2009) 1839, <http://dx.doi.org/10.1007/s10856-009-3763-8>.
- [39] L.E. Murr, S. Gaytan, F. Medina, H. Lopez, E. Martinez, B. Machado, D. Hernandez, L. Martinez, M. Lopez, R. Wicker, J. Bracke, Next-generation biomedical implants using additive manufacturing of complex, cellular and functional mesh arrays, *Phil. Trans. R. Soc. A* 368 (1917) (2010) 1999–2032, <http://dx.doi.org/10.1098/rsta.2010.0010>.
- [40] S. Yang, K.-F. Leong, Z. Du, C.-K. Chua, The design of scaffolds for use in tissue engineering. Part II. Rapid prototyping techniques, *Tissue Eng.* 8 (1) (2002) 1–11, <http://dx.doi.org/10.1089/107632702753503009>.
- [41] K. Svanberg, The method of moving asymptotes—a new method for structural optimization, *Internat. J. Numer. Methods Engrg.* 24 (2) (1987) 359–373, <http://dx.doi.org/10.1002/nme.1620240207>.
- [42] O. Amir, N. Aage, B. Lazarov, On multigrid-CG for efficient topology optimization, *Struct. Multidiscip. Optim.* 49 (2014) 815–829, <http://dx.doi.org/10.1007/s00158-013-1015-5>.
- [43] J. Wu, C. Dick, R. Westermann, A system for high-resolution topology optimization, *IEEE Trans. Vis. Comput. Graphics* 22 (3) (2016) 1195–1208, <http://dx.doi.org/10.1109/TVCG.2015.2502588>.
- [44] P. Coelho, P. Fernandes, J. Guedes, H. Rodrigues, A hierarchical model for concurrent material and topology optimisation of three-dimensional structures, *Struct. Multidiscip. Optim.* 35 (2008) 107–115, <http://dx.doi.org/10.1007/s00158-007-0141-3>.
- [45] L. Xia, P. Breitkopf, Concurrent topology optimization design of material and structure within FE2 nonlinear multiscale analysis framework, *Comput. Methods Appl. Mech. Engrg.* 278 (2014) 524–542, <http://dx.doi.org/10.1016/j.cma.2014.05.022>.

- [46] A.D. Cramer, V.J. Challis, A.P. Roberts, Microstructure interpolation for macroscopic design, *Struct. Multidiscip. Optim.* 53 (3) (2016) 489–500, <http://dx.doi.org/10.1007/s00158-015-1344-7>.
- [47] Y. Wang, H. Xu, D. Pasini, Multiscale isogeometric topology optimization for lattice materials, *Comput. Methods Appl. Mech. Engrg.* 316 (2017) 568–585, <http://dx.doi.org/10.1016/j.cma.2016.08.015>.
- [48] E. Garner, H.M. Kolken, C.C. Wang, A.A. Zadpoor, J. Wu, Compatibility in microstructural optimization for additive manufacturing, *Addit. Manuf.* 26 (2019) 65–75, <http://dx.doi.org/10.1016/j.addma.2018.12.007>.
- [49] J. Wu, O. Sigmund, J. Groen, Topology optimization of multi-scale structures: A review, *Struct. Multidiscip. Optim.* 63 (3) (2021) 1455–1480, <http://dx.doi.org/10.1007/s00158-021-02881-8>.
- [50] S. Zhou, Q. Li, Design of graded two-phase microstructures for tailored elasticity gradients, *J. Mater. Sci.* 43 (15) (2008) 5157–5167, <http://dx.doi.org/10.1007/s10853-008-2722-y>.
- [51] Y. Wang, F. Chen, M.Y. Wang, Concurrent design with connectable graded microstructures, *Comput. Methods Appl. Mech. Engrg.* 317 (2017) 84–101, <http://dx.doi.org/10.1016/j.cma.2016.12.007>.
- [52] H. Li, Z. Luo, L. Gao, P. Walker, Topology optimization for functionally graded cellular composites with metamaterials by level sets, *Comput. Methods Appl. Mech. Engrg.* 328 (2018) 340–364, <http://dx.doi.org/10.1016/j.cma.2017.09.008>.
- [53] Z. Du, X.-Y. Zhou, R. Picelli, H.A. Kim, Connecting microstructures for multiscale topology optimization with connectivity index constraints, *J. Mech. Des.* 140 (11) (2018) 111417, <http://dx.doi.org/10.1115/1.4041176>.
- [54] H.M. Kolken, S. Janbaz, S.M. Leeftang, K. Lietaert, H.H. Weinans, A.A. Zadpoor, Rationally designed meta-implants: a combination of auxetic and conventional meta-biomaterials, *Mater. Horiz.* 5 (1) (2018) 28–35, <http://dx.doi.org/10.1039/C7MH00699C>.
- [55] N. Ghavidelnia, M. Bodaghi, R. Hedayati, Femur auxetic meta-implants with tuned micromotion distribution, *Materials* 14 (1) (2021) 114, <http://dx.doi.org/10.3390/ma14010114>.
- [56] G. Dong, Y. Tang, Y.F. Zhao, A 149 line homogenization code for three-dimensional cellular materials written in matlab, *J. Eng. Mater. Technol.* 141 (1) (2019) 011005, <http://dx.doi.org/10.1115/1.4040555>.
- [57] M. Itagaki, Lower extremity CTS, 2020, URL <https://www.embodi3d.com>.
- [58] M. Heller, G. Bergmann, J.-P. Kassi, L. Claes, N. Haas, G. Duda, Determination of muscle loading at the hip joint for use in pre-clinical testing, *J. Biomech.* 38 (5) (2005) 1155–1163, <http://dx.doi.org/10.1016/j.jbiomech.2004.05.022>.
- [59] N. Moës, J. Dolbow, T. Belytschko, A finite element method for crack growth without remeshing, *Internat. J. Numer. Methods Engrg.* 46 (1) (1999) 131–150, [http://dx.doi.org/10.1002/\(SICI\)1097-0207\(19990910\)46:1<131::AID-NME726>3.0.CO;2-J](http://dx.doi.org/10.1002/(SICI)1097-0207(19990910)46:1<131::AID-NME726>3.0.CO;2-J).
- [60] S.A. Khanoki, D. Pasini, Fatigue design of a mechanically biocompatible lattice for a proof-of-concept femoral stem, *J. Mech. Behav. Biomed. Mater.* 22 (2013) 65–83, <http://dx.doi.org/10.1016/j.jmbbm.2013.03.002>.
- [61] G. Saravana Kumar, S.P. George, Optimization of custom cementless stem using finite element analysis and elastic modulus distribution for reducing stress-shielding effect, *Proc. Inst. Mech. Eng. H* 231 (2) (2017) 149–159, <http://dx.doi.org/10.1177/0954411916686125>.
- [62] J.A. Rand, M. Coventry, Stress fractures after total knee arthroplasty, *J. Bone Joint Surg.* 62 (2) (1980) 226–233.
- [63] A. Chamay, Mechanical and morphological aspects of experimental overload and fatigue in bone, *J. Biomech.* 3 (3) (1970) 263–270, [http://dx.doi.org/10.1016/0021-9290\(70\)90028-X](http://dx.doi.org/10.1016/0021-9290(70)90028-X).
- [64] R. Huijskes, H. Weinans, H. Grootenboer, M. Dalstra, B. Fudala, T. Slooff, Adaptive bone-remodeling theory applied to prosthetic-design analysis, *J. Biomech.* 20 (11–12) (1987) 1135–1150, [http://dx.doi.org/10.1016/0021-9290\(87\)90030-3](http://dx.doi.org/10.1016/0021-9290(87)90030-3).
- [65] A. Clemow, A. Weinstein, J. Klawitter, J. Koeneman, J. Anderson, Interface mechanics of porous titanium implants, *J. Biomed. Mater. Res.* 15 (1) (1981) 73–82, <http://dx.doi.org/10.1002/jbm.820150111>.
- [66] J.E. Davies, E. Ajami, R. Moineddin, V.C. Mendes, The roles of different scale ranges of surface implant topography on the stability of the bone/implant interface, *Biomaterials* 34 (14) (2013) 3535–3546, <http://dx.doi.org/10.1016/j.biomaterials.2013.01.024>.
- [67] O. Hoffman, The brittle strength of orthotropic materials, *J. Compos. Mater.* 1 (2) (1967) 200–206, <http://dx.doi.org/10.1177/002199836700100210>.
- [68] J.L. Stone, G.S. Beaupre, W.C. Hayes, Multiaxial strength characteristics of trabecular bone, *J. Biomech.* 16 (9) (1983) 743–752, [http://dx.doi.org/10.1016/0021-9290\(83\)90083-0](http://dx.doi.org/10.1016/0021-9290(83)90083-0).
- [69] R.L. Austman, J.S. Milner, D.W. Holdsworth, C.E. Dunning, The effect of the density–modulus relationship selected to apply material properties in a finite element model of long bone, *J. Biomech.* 41 (15) (2008) 3171–3176, <http://dx.doi.org/10.1016/j.jbiomech.2008.08.017>.
- [70] V. Eremeyev, A. Skrzat, F. Stachowicz, Linear micropolar elasticity analysis of stresses in bones under static loads, *Strength Mater.* 49 (4) (2017) 575–585, <http://dx.doi.org/10.1007/s11223-017-9901-5>.
- [71] S. Arabnejad, D. Pasini, Mechanical properties of lattice materials via asymptotic homogenization and comparison with alternative homogenization methods, *Int. J. Mech. Sci.* 77 (2013) 249–262, <http://dx.doi.org/10.1016/j.ijmecsci.2013.10.003>.
- [72] D.J. Berry, R.A. Berger, J.J. Callaghan, L.D. Dorr, P.J. Duwelius, M.A. Hartzband, J.R. Lieberman, D.C. Mears, Symposium: Minimally invasive total hip arthroplasty, *J. Bone Joint Surg.* 85 (11) (2003) 2235–2246.
- [73] J.T. Kim, J.J. Yoo, Implant design in cementless hip arthroplasty, *Hip Pelvis* 28 (2) (2016) 65–75, <http://dx.doi.org/10.5371/hp.2016.28.2.65>.
- [74] C. Balletti, M. Ballarin, F. Guerra, 3D printing: State of the art and future perspectives, *J. Cult. Herit.* 26 (2017) 172–182, <http://dx.doi.org/10.1016/j.culher.2017.02.010>.
- [75] G. Bergmann, F. Graichen, A. Rohlmann, Hip joint forces in sheep, *J. Biomech.* 32 (8) (1999) 769–777.